THE USE OF OPTICAL PROJECTION TOMOGRAPHY TECHNIQUE FOR TOMOGRAPHIC IMAGING OF MICE SKULLS

by

Spyridon Stavroulakis

An Undergraduate Thesis

Submitted to the Department of Physics

University of Crete

In Fulfillment of the Requirements

For an Undergraduate Degree

October 2023

Contents

1. Abstract

Now at a time when we can use relatively new imaging techniques to study whole rodent organs as small as a few centimeters. Such a method is mesoscopy. An important technique in this field is optical projection tomography (OPT). In this paper we review the use of the OPT technique, assisted by fluorescence, on biological specimens to study craniosynostosis disease. These biological samples consist of processed mice skulls. We analyze the principles of the OPT method, focusing on the filtered-back projection algorithm, which is the basic tomographic method for object reconstruction. We apply the use of optical projection tomography for full 3D reconstruction of 6 prepared skulls. Initially, the skull is reconstructed using OPT, with the help of LED illumination, calculating the light intensity before and after the light is absorbed by the specimen. Due to limitations faced in terms of analytical study of skull anatomy, we added the concept of fluorescence microscopy, where the regions of high interest in the specimen are also the fluorescent markers. The instruments and experimental setup we used in the experiments are presented, as well as the preparation of each specimen before the acquisition of the images. As an extension of the preceding, the importance of the number of projections on the quality of the reconstructed image is explained. Although we encountered some difficulties in isolating the spectra of the two fluorescent markers using filters alone, we examined the value of the Linear Unmixing method for separating fluorescent signals and quantifying cartilage and bone relative to the whole mouse skull. Finally, considering the results of the experiments, we study the shape of the cartilage that separates the bones of the skull from each other and thus our conclusions about craniosynostosis disease are drawn.

2. Introduction

2.1 Mesoscopy

The world of mesoscopy lies between that of microscopy and macroscopy. It involves the presentation of details in organs of a few centimeters. Mesoscopic imaging is an important field in the area of bioimaging and visualizes gross and fine tissue structures such as the trachea in the lung (diameter: 1.5 mm) , or intestinal villi (diameter: 200-500 μm). Today, there are several imaging techniques in the mesoscopic range such methods include micro-CT, which is widely used to detect cancer in small animals. It can provide resolution at about 50 μm in whole rodents and is sensitive to in vivo imaging of tumors. Another type of method is micro-MRI, which is considered the equivalent of MRI for visualizing small animals and is non-invasive without any use of harmful radiation. Moreover, due to the latter, this techniques preferred for imaging regions of the brain, nerves and spine. It provides higher resolution in ligament, muscle and tendon images than X-ray or micro-CT, and thus is even favored in knee and shoulder case. The high resolution may be achieved by increasing the intensity of the magnetic field. (1)

Unfortunately, the cost of the experimental tools, the above imaging methods, and their maintenance is very high, making their use less common. However, these two are a small portion of the wide variety of mesoscopic imaging. Other such examples:

- Functional ultrasound imaging (fUS), which measures the echoes from the sound waves transmitted through the instrument to obtain three-dimensional images in vivo (resolution up to 100 μm),
- Bioluminescence imaging (BLI), based on the detection of chemically induced fluorescence. This method is also used for the detection of cancerous tumors in small animals in vivo (resolution at approximately 1 mm),
- Optoacoustic tomography (OA), which detects ultrasound upon absorption of an excitation beam, increasing the resolution of the detected signal in deep tissues (resolution at 100 μm),
- and Ultramicroscopy in which a thin sheet of light, produced by one or more cylindrical lenses, illuminates the sample from the side. (2)

Optical projection tomography (OPT) belongs to this category of mesoscopic imaging, combining some of the above methodologies with the idea of low maintenance costs of the necessary equipment.

2.2 Optical Projection Tomography

Optical projection tomography, also called optical computed tomography (optical-CT), is a revolutionary new 3D imaging technique for big biological samples (on the order of one cubic centimeter). This method, developed by James Sharpe, is mainly used to reconstruct vertebrate embryos using light emitted from inside the specimen through fluorescence. OPT has come to fill the gap between magnetic resonance imaging (MRI) and conventional microscopy. More specifically, it has the ability to image specimens at a higher resolution than MRI and at the same time the size of these specimens is much larger than was possible using confocal laser-scanning microscopy. In addition, this technique is revolutionary because, unlike others, it is not necessary to physically cross-section the sample, thus making the procedure simpler. Furthermore, optical projection tomography is able to take advantage of many fluorescent dyes, which were created to stain very specific tissues or proteins (3). Thus, channels of different wavelengths can be used. This allows the computer to observe the autofluorescence of the tissue as well as to automatically determine the contours of the desired structure of the 3D sample.

Our main goal is to use e-OPT and t-OPT to observe craniosynostosis disease in mouse embryo skulls. More specifically, our issue is the distinct detection of skull sutures so that we can confidently infer whether they were suffering from this disease, based on a low-cost method. (4)

2.2.1 Limitations

Optical Projection Tomography (OPT) is a valuable imaging technique, particularly in the fields of biology and material science, but it does come with notable limitations. One primary constraint is its restricted applicability to transparent or semi-transparent samples. OPT

struggles to provide meaningful data for opaque or highly scattering specimens, limiting its versatility in studying a wide range of materials. Furthermore, the depth of penetration is a crucial limitation, as the imaging quality diminishes with increasing sample thickness. That restriction means that OPT may not be the ideal choice for visualizing structures within thick, densely packed samples.

Another limitation is the resolution offered by OPT, which is typically lower than that of some other high-resolution imaging methods like confocal microscopy or electron microscopy. This can hinder the ability to capture fine details, making it less suitable for studies requiring precise visualization of intricate structures. Additionally, OPT may not be the best choice for rapidly changing or dynamic processes due to its relatively slow imaging speed. Despite these limitations, OPT remains a valuable tool for many scientific investigations, particularly when clear, transparent samples are involved, and researchers carefully consider its strengths and weaknesses in their specific applications. (5)

2.3 Craniosynostosis

The skulls of newborns are divided by various flexible seams into individual plates. These seams, as the embryos grow and the brain develops, close, turning the plates and seams into a single bone. (6)

Craniosynostosis is a disease that occurs in newborns in which one or more of the fibrous sutures close prematurely causing severe problems in skull and brain development. The truth is that many times the structure of the skull can be such that brain development is allowed, only to result in an abnormal formation of head features. This is because the skull cannot grow perpendicular to the joined sutures and compensates for this limitation by growing more than normal alongside them, thus creating this unusual shape. In other cases, where the skull is not allowed this kind of growth either, so much pressure is exerted internally that it can create irreversible problems for the patient, such as weaknesses in vision, sleep and mental problems.

Craniosynostosis is common and occurs approximately in one out of 2,200 births. Furthermore, it happens more often to males than females and can be inherited in some families. Early diagnosis is vital as it can be treatable. The only treatment provided is surgery, through which it will reduce the pressure inside the skull by correcting the deformities of the skull itself. The appropriate age to be operated on is that of less than one year old, as the skull is still soft and thus more easily managed by doctors. After successful surgery, infants are required to be under constant observation in rehabilitation centers. Moreover, re-synostosis after standard surgical procedures for no syndromic craniosynostosis is a rare event, which can occur at the same suture or rarely in adjacent sutures. (7)

3. Materials & Methods

3.1 Tomographic Reconstruction

3.1.1 Beer-Lambert Law

When the sample is transparent then with the help of LED illumination the CCD records a dark version of the sample. This is because the bones and thicker tissues absorb a very large part of the emitted light. At the same time, we can also see some brighter parts in the sample, such as the central part of the skull, which is made up of a thinner tissues that does not absorb a large amount of radiation. In addition, we record an image of the emitted light without the sample in order to compare the differences in light intensity. The law that describes this phenomenon, measuring the absorption of light as it travels through the sample, relating it to various properties of the sample is the Beer-Lampert law. It is described by the equation:

$$A = log_{10}\frac{I}{I_0} = \mu \cdot L \quad (1)$$

where I is the intensity of the light after it has travelled a distance of length L of the sample, I_0 is the initial intensity of the light and μ is a radiation-sample absorption constant. (2)

3.1.2 Radon Transform

More generally in the science of mathematics, the Radon Transform is an integral transformation that turns a function f, defined on a plane, into a function R_θ defined in the two-dimensional line space of the plane. The function R_θ, in particular, computes the projections of an image matrix of specified directions. For example, a function f(x,y), defined in 2D, consists of a set of linear integrals. Thus, the Radon function, R_θ, computes linear integrals from multiple sources along these parallel paths in a specified direction specified by the angle θ (8). This transformation was first presented in 1917 by the Austrian mathematician Johann Radon, whose work was to play a key role in the invention of Computed Tomography(CT) (9). In biological imaging systems, projections are measured through a density object f(x,y) and these projections R_θ, are computed by integrating along the direction where each projection is collected (i.e. along the direction of the arrows in **figure 1**). An easily and directly applicable mathematical form of the Radon Transform is done via the delta function and is written:

$$R_\theta(f,\theta,t) = \iint_{-\infty}^{\infty} f(x,y)\delta(xcos\theta + ysin\theta - t)dxdy \quad (2)$$

where θ is an arbitrary angle from which the light passes through the sample f(x,y).

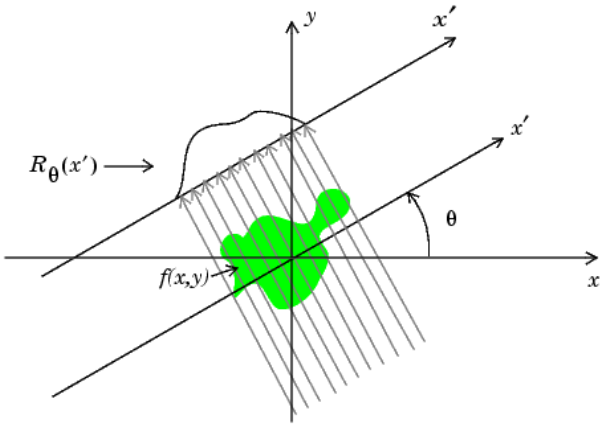

***Figure 1**: The Radon Transform of a 2D segment f(x,y) projected onto a linear integral R_ϑ at a random angle ϑ* (10).

However, from **figure 1** we can deduce the significant limitations of X-rays in the sense of dimensionality, due to the lack of depth. For this very reason it is worth commenting on the use of the time parameter t in equation (4). It is easy to think that you cannot fully perceive the morphology of a shadow in space. Nevertheless, if it starts to rotate around itself, by taking projections, we can obtain more information about the structure of that shadow.

This is exactly the logic of the CT operation. To eliminate these limitations due to lack of depth, we take projections of the sample from different angles at a 180° interval. And so, the full 3D reconstruction of the object will result from the inverse of the Radon Transform, which is of the form:

$$f_{bp}(x,y) = \int_0^\pi R_\theta(xcos\theta + ysin\theta)d\theta \quad (3)$$

where the function f_{bp} represents the three-dimensional reconstruction of the sample with the characteristic name back-projection, whose algorithm will be discussed in more detail in the following paragraphs. More generally, using the inverse of the radon transform on each part of the object will give us the reconstruction of the whole sample. The quality of the reconstruction is strongly characterized by the number of projections. The more projections we obtain, the better sense we will have of the sample morphology.

All of the above is summarized in the following images showing two examples of reconstructing a mouse skull with the back-projection algorithm. First, we take three projections from different angles by calculating their linear integrals $R_{\frac{1}{9}\pi}(t)$, $R_{\frac{4}{9}\pi}(t)$ και $R_{\frac{7}{9}\pi}(t)$, as shown in **figure 2(a)**. Then, in **figure 2(b)**, the Radon Transform process is reversed and each projection is copied and displayed in the reconstruction space in the opposite direction of the original projection (2). As can be seen, in this case, the shape of the mind is hardly perceptible, due to the minimal information that the set of projections gives us about

the depth of the sample. In the second case, in **figure 2(c)**, the projections in the sample are 600, i.e. one projection per 0.3°, which results in a much sharper view of the sample. However, the morphology of the brain appears quite blurred, perceiving little detail. That happens because of the oversampling at the center and less sampling at the edge.

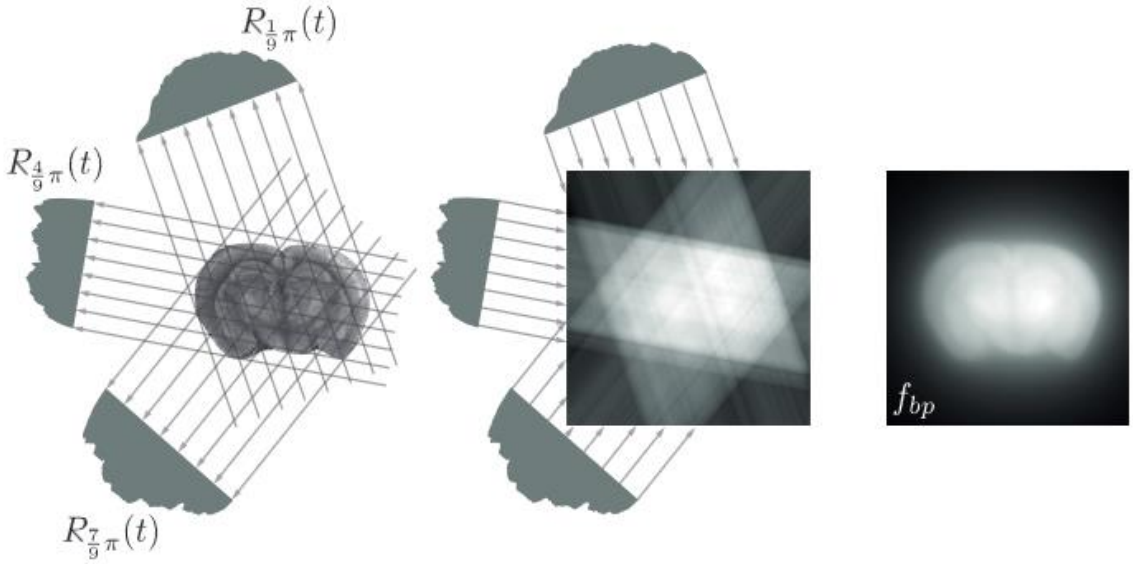

(a) (b) (c)

***Figure 2**: **(a)** Obtain three projections of a mouse brain from three different angles, represented as the linear integrals $R_{\frac{1}{9}\pi}(t)$, $R_{\frac{4}{9}\pi}(t)$, $R_{\frac{7}{9}\pi}(t)$. **(b)** After obtaining the projections, then the reverse procedure takes effect and these three projections are copied and redirected in the opposite direction to the reconstruction plane.**(c)** The complete reconstruction of the sample, f_{bp}, generated by a projection acquisition rate of 1 projection per 0.3°.* (2)

An effective method to eliminate these inaccuracies and get more elegant and sharp details in the sample images is through filtering, during back-projections. This technique is called filtered back-projection and its analysis requires knowledge of the next theorem we will deal with, the Central Slice Theorem.

3.1.3 Central Slice Theorem

The Central Slice Theorem, or projection-slice theorem, is perhaps the most important mathematical theorem in the field of computed tomography and is a step that unites the Radon Transform with the Fourier Transform. The relationship that defines this theorem is as follows:

$$\hat{f}_{pol}(\omega, \theta) = \hat{R}_{\theta}(\omega) \quad (4)$$

where $\hat{f}_{pol}$ is the two-dimensional Fourier transform at the polar coordinates (ω,θ) and $\hat{R}_\theta$ is the one-dimensional Fourier transform of the linear integral from the Radon transform at the corresponding angle θ. (2)

In particular, the Central Slice Theorem tells us that an infinite number of Fourier-transformed linear integrals is equivalent to the 2D Fourier transform, $\hat{f}$, of an object segment. This allows for an alternative way of reconstructing any section of the object section. More specifically, at first we collect the projections from a central section of the sample, then we compute the Fourier Transform for each of them, and after the 2D spectrum is generated, finally the inversion of the Fourier transform in two dimensions this section. On the other hand, the number of Fourier transformed linear integrals is finite and this limits the Fourier domain. This theorem further provides the means by which the linear integrals are filtered in the field and introduces us to the Filtered Back-Projection.

3.1.4 Filtered Back-Projection

As we have seen, filtered back-projection is an accurate reconstruction algorithm that was designed from the outset to counteract the limitations created by a conventional back-projection reconstruction method. The algorithm utilizes equations of rays, obtained at different angles through the projections, to calculate the values of the attenuation coefficients within a section. (11) (2)

The truth is that it results from the inverse of the 2D Fourier transform, which has the form:

$$f(x,y) = \frac{1}{(2\pi)^2}\iint_{-\infty}^{\infty} \hat{f}(\omega_x,\omega_y)e^{i(\omega_x x+\omega_y y)}d\omega_x d\omega_y \quad (5)$$

where $\hat{f}$ is a 2D transformation of the function f defined in the Cartesian frequency coordinates (ω_x,ω_y). A much more auxiliary form of the equation is in polar coordinates:

$$f(x,y) = \frac{1}{(2\pi)^2}\int_0^{2\pi}\int_0^{\infty} \omega\hat{f}_{pol}(\omega,\theta)e^{j\omega(xcos\theta+ysin\theta)}d\omega d\theta \quad (6)$$

where $\omega = \sqrt{\omega_x^2+\omega_y^2}$, $\theta = \arctan\frac{\omega_x}{\omega_y}$, and $\omega d\omega d\theta = d\omega_x d\omega_y$. Combining relation (6) from the Central Slice Theorem with relation (8) we get:

$$f(x,y) = \frac{1}{(2\pi)^2}\int_0^{2\pi}\int_0^{\infty} \omega\hat{R}_\theta(\omega)e^{j\omega(xcos\theta+ysin\theta)}d\omega d\theta \quad (7)$$

In order to derive the required algorithm we now divide the integration into a range of angles 0 to π and from π to 2π. Let, f_1 and f_2 be the integrals with new boundaries for which $f(x,y) = f_1 + f_2$. Thus:

$$f_1(x,y) = \frac{1}{(2\pi)^2}\int_0^{\pi}\int_0^{\infty} \omega\hat{R}_\theta(\omega)e^{j\omega(xcos\theta+ysin\theta)}d\omega d\theta \quad (8)$$

and similarly:

$$f_2(x,y) = \frac{1}{(2\pi)^2}\int_{\pi}^{2\pi}\int_{0}^{\infty} \omega \hat{R}_{\theta}(\omega) e^{j\omega(x\cos\theta + y\sin\theta)} d\omega d\theta \quad (9)$$

To form the desired range of angles (0,π) in the second integration we can set a new angle $\theta \rightarrow \theta - \pi$ and write:

$$f_2(x,y) = \frac{1}{(2\pi)^2}\int_{0}^{\pi}\int_{0}^{\infty} \omega \hat{R}_{\theta-\pi}(\omega) e^{j\omega(x\cos(\theta-\pi) + y\sin(\theta-\pi)} d\omega d\theta \quad (10)$$

and relation (12) is rewritten:

$$f_2(x,y) = \frac{1}{(2\pi)^2}\int_{0}^{\pi}\int_{0}^{\infty} \omega \hat{R}_{\theta-\pi}(\omega) e^{-j\omega(x\cos\theta + y\sin\theta)} d\omega d\theta \quad (11)$$

Finally, we know that the symmetry holds:

$$\hat{R}_{\theta-\pi}(\omega) = \hat{R}_{\theta}(-\omega) \quad (12)$$

So, relation (13) will be written:

$$f_2(x,y) = \frac{1}{(2\pi)^2}\int_{0}^{\pi}\int_{0}^{\infty} \omega \hat{R}_{\theta}(-\omega) e^{-j\omega(x\cos\theta + y\sin\theta)} d\omega d\theta \quad (13)$$

And setting the frequency in the interval of negative values (-∞,0), then for (13) we have:

$$f_2(x,y) = \frac{1}{(2\pi)^2}\int_{0}^{\pi}\int_{-\infty}^{0}(-\omega) \hat{R}_{\theta}(\omega) e^{j\omega(x\cos\theta + y\sin\theta)} d\omega d\theta \quad (14)$$

Therefore, the final form of equation (7) corresponds to the sum of relation (8) and relation (14), i.e.:

$$f_{bp}(x,y) = \frac{1}{(2\pi)^2}\int_{0}^{\pi}\int_{-\infty}^{\infty}|\omega| \hat{R}_{\theta}(\omega) e^{j\omega(x\cos\theta + y\sin\theta)} d\omega d\theta \quad (15)$$

Relation (15) is the algorithm of the filtered back-projection. From there we observe that the above relation is equivalent to a back-projection of relation (3) where each linear integral is Fourier transformed, multiplied by the frequency $|\omega|$ and transformed back into the back-projection domain. (2)

That last equation involves a filtering process, where the term $|\omega|$ represents the frequency response of the filter. It is well known that back-projection causes higher density in the regions close to the origin, lower density farther than the origin, correspondingly higher spatial frequencies are suppressed by means of $1/|\omega|$. However, a $|\omega|$ filter can improve it. (12)

The filter transfer function H, defined as

$$H(\omega) = |\omega| \quad (16)$$

is called Ram-Lak filter and describes a ramp that emphasizes the high spatial frequencies in a sinogram from noise-free projections in order to obtain a sharper reconstruction in the back-projection process.

Another type of filter is the Shepp-Logan filter, which is obtained by the multiplication of the Ram-Lak filter and the cardinal sin function: $\{sinc(x) = \frac{sinx}{x}\ , x \neq 0\}$

$$H_{Shepp-Logan}(\omega) = |\omega| sinc(\omega) \quad (17)$$

where its use lies in the fact that at high spatial frequencies it attenuates its gain resulting in noise removal. (2)

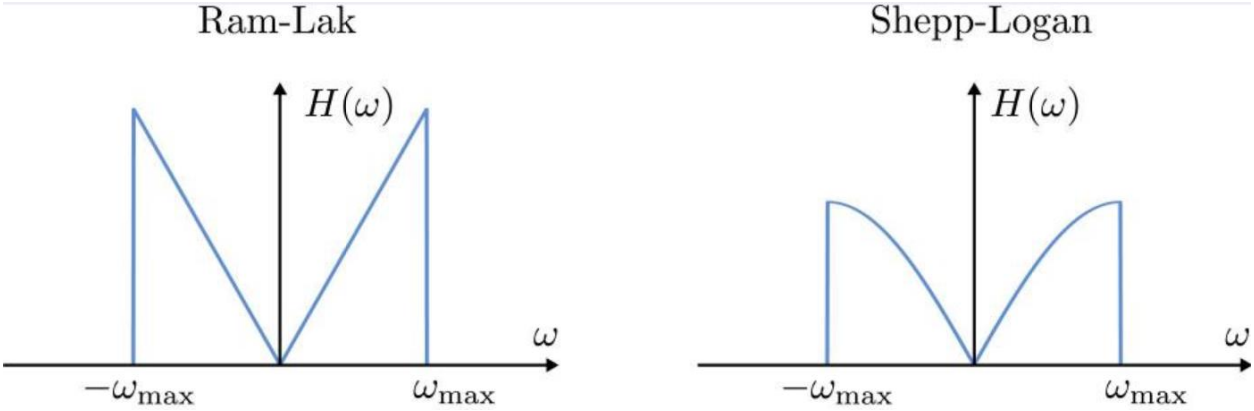

Figure 5: *The filter transfer diagrams of the FBP algorithm are shown. In general, the Ram-Lak filter is used to reconstruct our image without noise. High spatial frequencies in the line integrals are linearly emphasized by $|\omega|$, in order to give more emphasis to the acquired projections and form a better reconstruction. However, the projections we obtain already are corrupted by high spatial frequency noise and by using the Ram-Lak filter, that noise would be emphasized. To compensate for this effect, the Shepp-Logan filter is used. That filter is like the Ram-Lak filter combined with a sinc function, which has the property at high frequency values to attenuate the gain.* (13)

So, a simple summary of the FBP algorithm is as follows: (I) Acquire projections from object, (II) take 1D Fourier transform and apply $|\omega|$ filter, (III) calculate inverse 1D Fourier transform, (IV) have back-project result.

These operating steps of the FBP algorithm are illustrated in **figure 6** where the brain shape of a mouse is shown in **figure 6(a)**. Initially, in **figure 6(a)** we acquire the linear integrals from different angles over 180^o by performing the Radon transform. In **figure 6(b)** the sinogram is formed, which is the graphical representation of that 2D Radon transform. This graph consists of the columns of the matrix of these linear integrals. Then the sinogram is filtered column by

column in the Fourier domain with a ramp, as clearly shown in **figure 6(c)**, and finally in **figure 6(d)** the filtered sinogram is projected back creating a complete and detailed reconstruction of the sample.

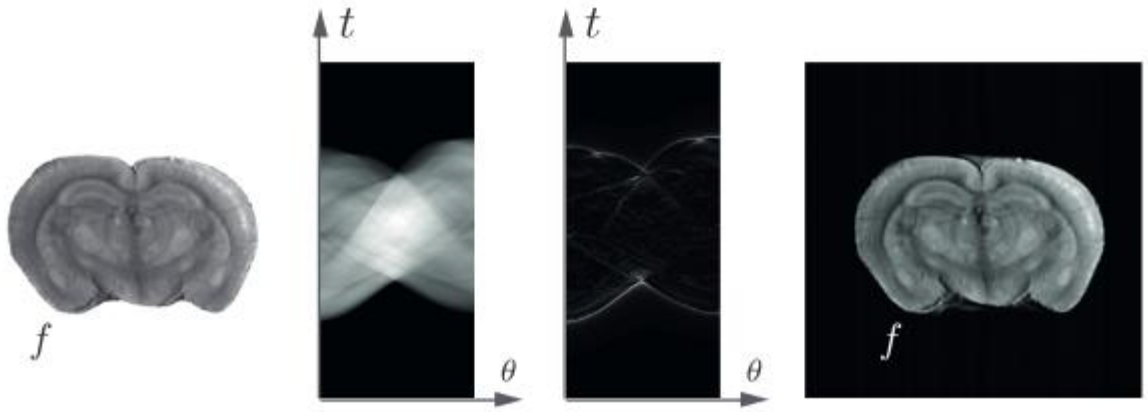

(a) (b) (c) (d)

Figure 6: *The steps in the process of running the filtered back-projection algorithm.* ***(a)*** *The projections, i.e. line integrals, of the sample from different angles are collected.* ***(b)*** *Each of the line integrals are placed in columns of a matrix, which is called a sinogram.* ***(c)*** *The sinogram is filtered column by column with the help of a ramp in Fourier domain* ***(d)*** *Finally, the back-projection of the filtered sinogram is illustrated which leads to a complete and detailed reconstruction of the mouse's brain.* (2)

Here is also shown the sinogram shape in the mouse embryo skull case (S024) which is mixed colored with both fluorophores.

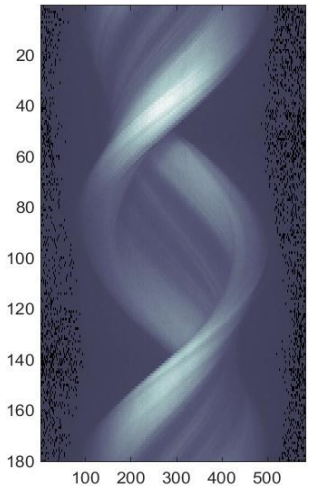

Figure 3*: Sinogram of sample 024 under the 635 nm excitation beam with a 700 nm long pass emission filter.*

3.2 T-OPT & F-OPT Modes

Optical Projection Tomography is a valuable tool for researchers in the life sciences who require 3D imaging of biological samples without damaging or dissecting them. Its non-invasive nature and ability to provide detailed internal structural information make it a valuable technique for a wide range of applications, from studying embryonic development to disease pathology. A general truth is that the optical projection tomography is considered to be roughly the optical equivalent of X-ray computed tomography, which uses a very similar technique, although we can see that there are some important differences.

In OPT's transmission mode, the format of the images we get from the sample depends strongly on the density of the constituent tissues. Different amounts of white light are absorbed by different tissues in the biological sample of interest. As a result, some tissues that do not absorb as much light are shown in grey, other areas that show high attenuation appear black and the background which is obviously white since there is no absorption. Unfortunately, this mode shows inaccuracies in structure just as X-rays do.

This gap was filled by the second function of optical projection tomography. In the fluorescence mode, an excitation laser beam strikes the appropriately stained biological sample so as to stimulate the fluorescence property in the labeled regions of interest. The CCD camera then detects fluorescence signals from the bright spots that fluoresce in the dark rest of the sample body. There are many types of fluorescent dyes that extend the applications of the fluorescence function in OPT to the biological sciences, such as the alcian blue and alizarin red dyes that we used in these experiments.

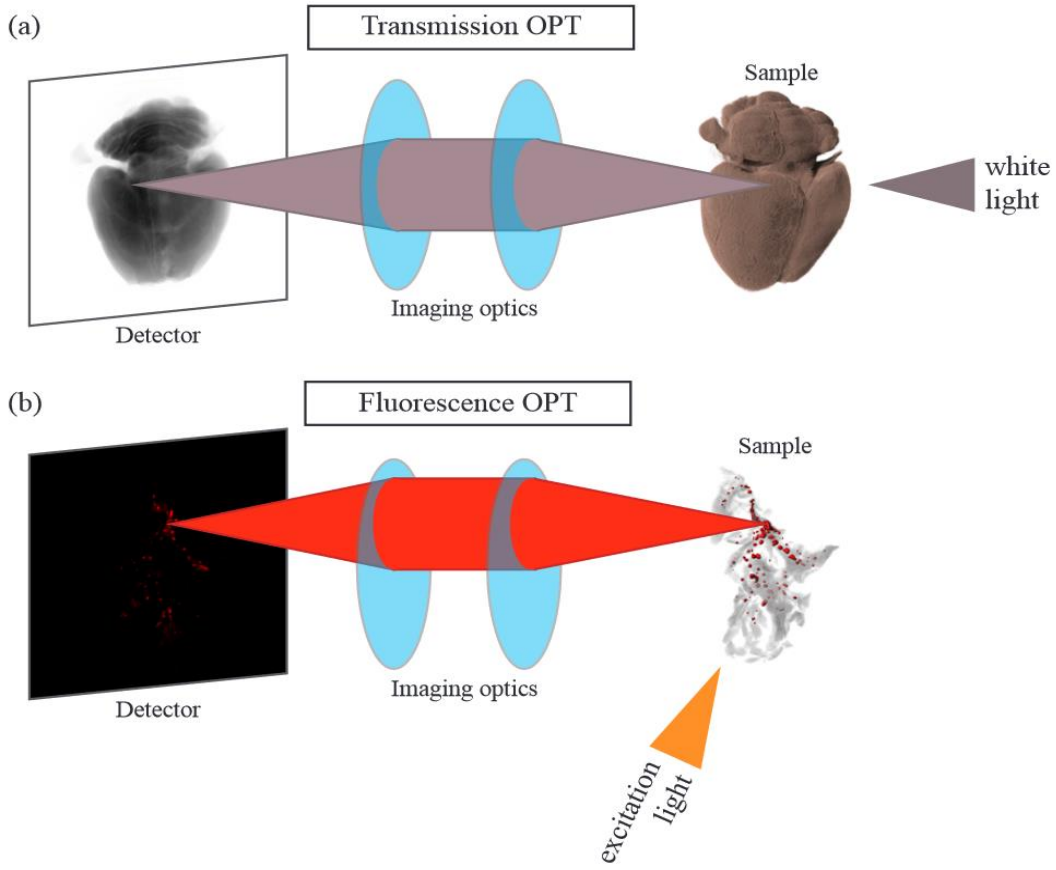

Figure 7: *The OPT is characterized by two modes: (a) transmission mode (t-OPT) and (b) fluorescence mode (f-OPT). In transmission mode white light is used to penetrate the sample, which is cleaned of the various hairs to avoid any scattering, and through the camera we acquire information about the structure of our biological sample. On the other hand in fluorescence mode, the sample is exposed to excitation laser beam emitting new channels of wavelengths giving us detailed information about the fundamental parts of the sample, such as proteins and tissues.* (2)

3.3 Experimental Set-up

- **T-OPT**

In transmission mode of OPT, the sample is illuminated with a collimated beam of light, typically in the visible or near-infrared spectrum. The sample is rotated incrementally, and a series of 2D projection images are captured at different angles as the light passes through the sample.

In our case, an evenly distributed LED illumination behind the sample was being used. Amount of light was being absorbed by the sample and the CCD camera was capturing images one after the other, essentially measuring this absorption.

- **E-OPT**

First, for f-OPT we used three different wavelengths from two different lasers. There is a He-Ne Laser at 635 nm (red beam) and an Ar^+ Laser both at 514 nm (green beam) and at 488 nm (blue beam) with their powers at the source and sample points shown in the table below:

	Power (mW)		
	Laser He-Ne (635nm)	Laser Ar^+ (514nm)	laser Ar^+ (488nm)
Source	26.1	25.2	12.4
Sample	12.5	8.8	2.7

For the Ar^+ laser beam directional design we first created the spatial filter array. A spatial filtering scheme must be appropriately, so that a pure Gaussian beam is produced by filtering out the remaining unwanted energy maxima and allowing only the central diffraction fringe to enter. In addition, it prevents the formation of unwanted rings in the laser profile due to light scattering caused by dust or other parts of the device. At the beginning, we use an aspheric lens to concentrate the beam at a single point where the pinhole is located. Next, the pinhole, of appropriate diameter, is the one that will isolate the desired clean central fringe for our experiment. (14)

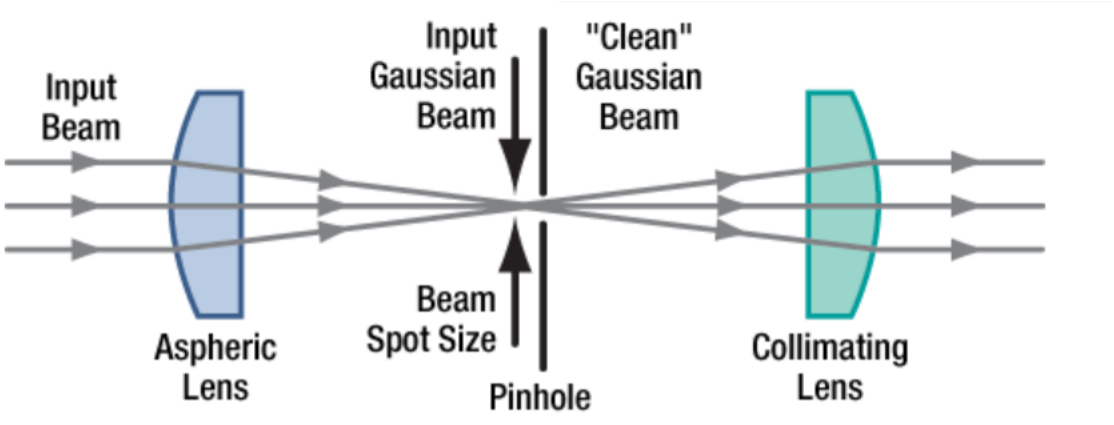

Figure 8: *Spatial Filter System*

It is known that the diameter of the first fringe to form is calculated from the equation:

$$D = \frac{\lambda \cdot f}{r} \quad (18)$$

Where D is the diameter of the first diffraction fringe, λ is the wavelength of the beam, f is the local length of the aspherical lens preceding the hole, and r is the radius of the incoming beam. For the Ar^+ laser we have a focal length of aspheric lens f=25mm and f=35mm for the He-Ne laser. The choice of the appropriate pinhole is such that its diameter is 30% larger than the D size, i.e. ≈1.3D (15). The placement of the suitable one is important, as if we place a smaller size than our theoretical value, then the fringe will be truncated, while if we place a pinhole of larger diameter than 1.3D, then more maxima will penetrate the pinhole than the first one. The table below shows our experimental values for the first fringes:

	D(mm)	Pinhole Diameter(μm)
Laser Ar^+ (488 nm)	15	20
Laser Ar^+ (514 nm)	15	20
Laser He-Ne (635 nm)	15	30

Finally, to adjust the final beam to the desired diameter, we place a focusing lens of a certain focal length at the appropriate distance. The value of the focal length of the focusing lens is determined by the desired diameter of the outgoing beam by means of the similar triangle theorem, which is shown in the diagram below:

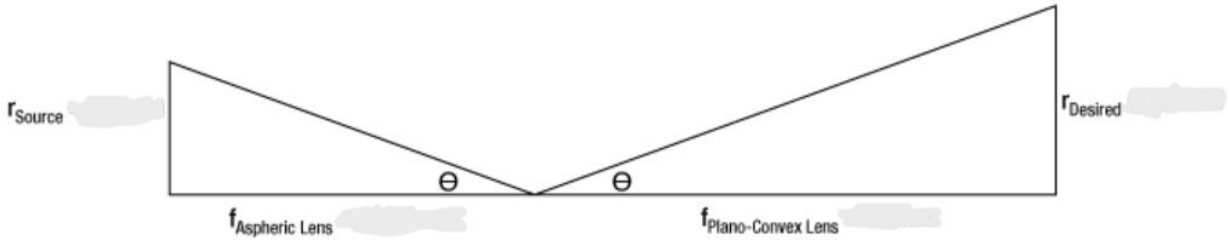

For a certain angle, whose value is determined by the left triangle and is approximately $\theta = tan^{-1}\frac{r_{source}}{f_{Aspheric\ Lens}} \approx$ and knowing approximately the desired diameter of the outgoing beam $r_{Desired}$, the focal length of the concentrating lens $f_{Plano\text{-}Convex\ Lens}$ to be used in our configuration is obtained by the following simple analogy:

$$f_{Plano-Convex\ Lens} = \frac{f_{Aspheric\ Lens} \cdot r_{Desired}}{r_{source}} \quad (19)$$

Thus, for the first Ar^+ laser for $r_{Desired}$=15mm, we placed a focusing lens of focal length f=60mm, and for the second Laser He-Ne for $r_{Desired}$=18mm we put another one with f=45mm.

We then added mirrors in both directions of the laser beams. So that we could bring them to a common mirror where from there they would be guided in a common direction to the sample point.

3.4 Types of Samples & Stains

To begin with, both in the transmission and fluorescence mode of OPT, it is essential for the sample to possess transparency or semi-transparency characteristics. Achieving this transparency often requires the application

The Department of Biology in Crete had prepared and provided us with six types of mouse embryo skulls, which we studied later at our experimental setup. These types of samples are divided into three groups of two according to the color that were dyed. The first two of them (No 11, No 12) were dyed with Alizarin Red pigment, the other two (No 15, No 25) were dyed with Alcian blue and the last skulls (No 14, No 24) had encounter both pigments.

Alcian blue is any member of a family of polyvalent basic dyes. It is generally used to stain acidic polysaccharides such as glycosaminoglycans in cartilage and other body structures, some types of mucopolysaccharides. The use of Alcian blue has been throughout the ages a popular staining technique in histology. It is used to visualize acidic epithelial and connective tissue mucins, where mucins are a type of carbohydrate. Furthermore, at quite high dilution, it has an absorption maximum of ~600-615 nm.

Alizarin Red S is a water-soluble sodium salt of Alizarin sulfonic acid. It is used for the staining of cartilage and bone and so we did in our samples. It is well known that Alizarin Red S reacts with calcium, thereby helping in the diagnosis of calcium deposits. Whole specimens can be stained with it to show the distribution of bone, especially in developing embryos.

The most important parts of these stains were both their absorption measurements in spectrophotometer and their fluorescence signals which were resulted by fluorimeter in I.T.E Department. In Alcian blue the fluorescence and absorbance diagram are shown below respectively (diag. 1.1, 1.2). Similarly for Alizarin red (diag. 1.3, 1.4).

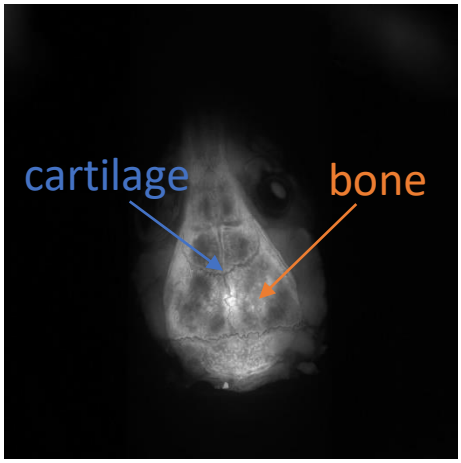

***Figure 9**: The image above shows the first direct 2D projection of a skull of the sample (S024), which is impregnated with both dyes, in the respective regions. **a)** The symmetrical lines, which are shown in bold from top to bottom, are the so-called seams separating the sections of the mouse embryo skull. As we have mentioned, these seams are painted with the dye alcian blue. **b)** The sections separated by these seams are the bones, which, as the brain develops and the seams close, will join together. The bone is stained with alizarin red. In addition, in this particular image a 615 nm filter FWHM of 90 nm has been placed on the camera lens and the beam with which we excited it was the Ar^+ Laser with a wavelength of 488 nm.*

In addition, for the diameter of our camera lens, we have 3 different filters available. We have a filter that allows the 540 nm FWHM (Full Width at Half Maximum) of 40 nm (520-560 nm) to pass through, the second at 615 nm FWHM of 90 nm (570-660 nm) and the third at 700 nm FWHM of 70 nm (665-735 nm). With this simple trick we can collect different information on the same sample.

We inserted through a pipette a few ml of a quantity of each dye into cubes and measured with the aid of the spectrophotometer the respective absorptions at a certain wavelength barrier.

3.5 Spectrophotometer

Simply put, the principle of operation of the spectrophotometer consists of four essential parts. The first part of the device comprises light source. The second part, consisting of the monochromator and an adjustable aperture, separates the desired wavelength from the rest of the wavelengths produced by the source. This monochromatic radiation is then incident on the sample, i.e. the cuvette, the third part. Finally, there is the radiation meter, where it measures the radiation that eventually passes through the sample, i.e. that which is not absorbed. (16)

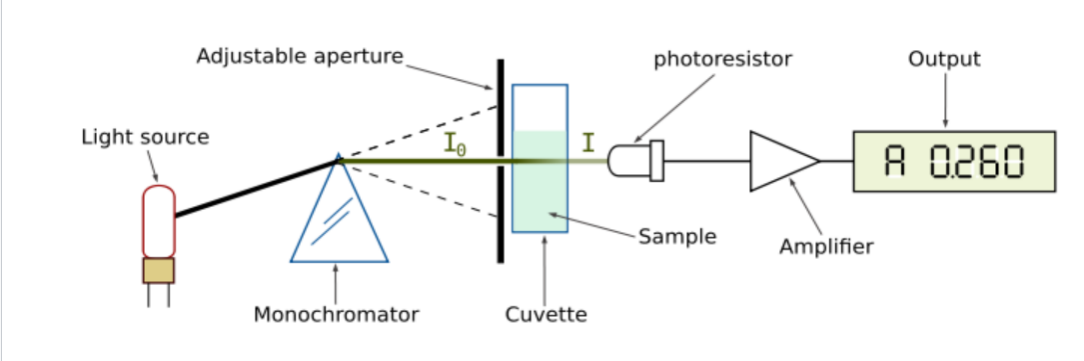

Figure 10: *Simplified experimental setup of a visible and ultraviolet spectrophotometer (UV-VIS).*

Below are the absorption and emission plots, in normalized form, of each dye in the sample, alizarin red localized in the bone region and alcian blue in the suture region, for the different laser excitation wavelengths.

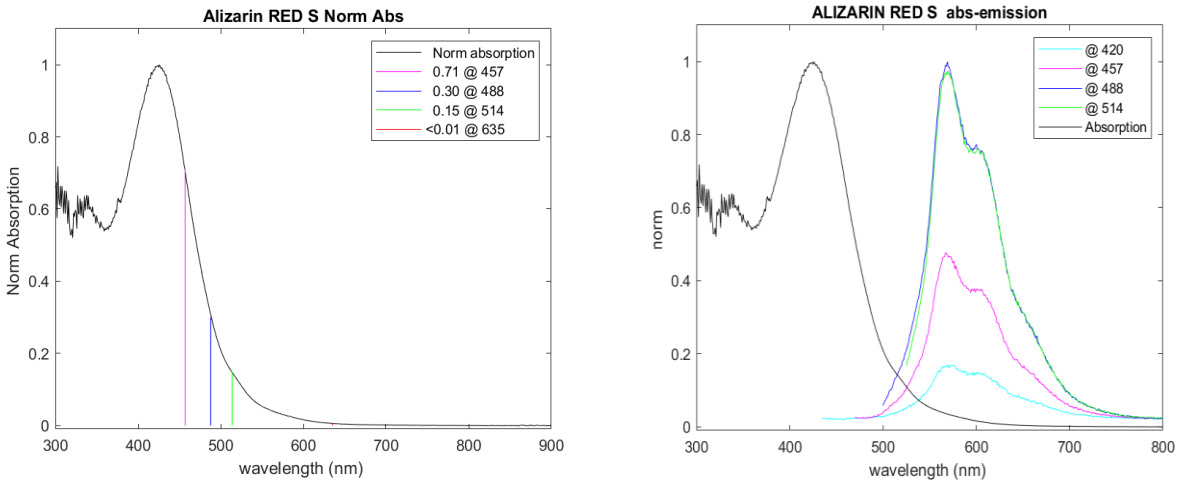

(a) *(b)*

Figure 10: *In both diagrams the black curve represents the normalized form the radiation absorption by the alizarin red dye. By a simple observation we understand that the value of the maximum absorption wavelength is 420 nm. In* ***figure 10 (a)****, the colored lines show the radiation absorption rates at the emitted wavelengths of high interest (71% for 457 nm, 30% for 488 nm, 15% for 514 nm and <0.1% for 635 nm). In* ***figure 10(b)****, the colored graphs show the radiation emission from alizarin red dye, for absorption of each desired wavelength.*

It is worth noting that alizarin red dye does not absorb any 635 nm wavelength beams. This makes perfect sense, since this value is in the red region. Furthermore, although theoretically a laser beam of 457 nm wavelength seems the most suitable to give us more information and details about the bone region in the skull, the low power of the Ar^+ Laser at this wavelength

value does not allow us to do so. In contrast, for the two skulls exclusively stained with alizarin red, we only considered the 488 nm and 514 nm laser beams.

Similarly, we placed a few ml of alcian blue dye in a cuvette and used the spectrophotometer for once more. We can see our results in the following absorbance graphs for the alcian blue dye.

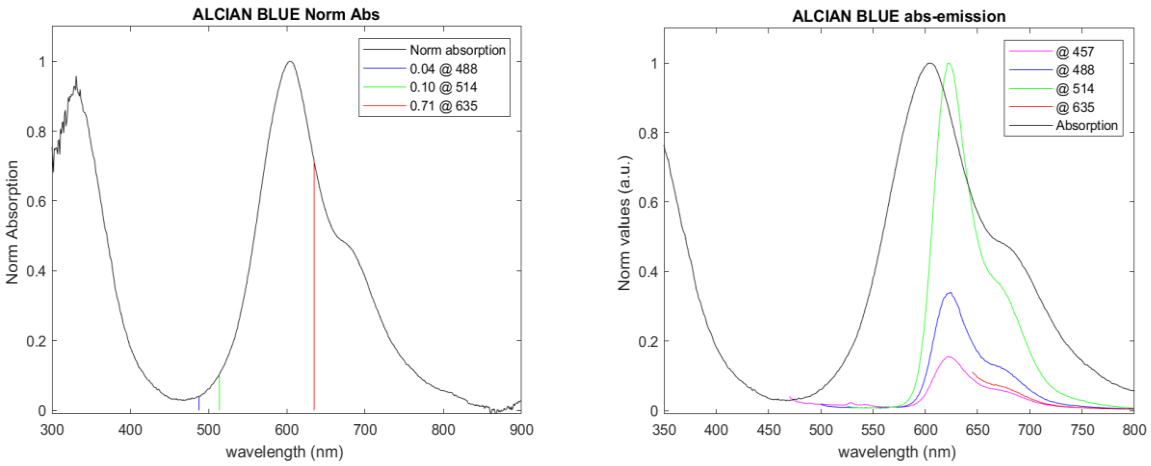

(c) *(d)*

Figure 11: *In the same way as for the alizarin red, the black curve depicts the absorption of radiation from the alcian blue dye.* ***Figure 11(c)*** *shows the absorption rates of selected wavelengths from the cuvette sample (~71% for 635 nm beam, ~10% for 514 nm beam, and ~4% for 488 nm beam). Finally* ***figure 11(d)*** *shows the amount of radiation emission from the sample, i.e. its fluorescence, for absorption of these selected wavelengths.*

It is easy to see that in the case of alcian blue, greater absorption occurs at 635 nm but at the same time there is no fluorescence in this region. Therefore, we can conclude that isssn the He-Ne Laser (635 nm).

Then, we used in the same way, next to the spextophotometer, the fluorometer setup which recorded the fluorescence intensity and the corresponding emission spectrum for each dye. In this way, we will know at which wavelength we can obtain more detail about the desired part of the skull (bone or cartilage), and therefore we will be able to isolate whichever wavelength range we really want, using the filters' channels.

3.6 Fluorometer

It is based on the method of fluorecsence spectroscopy, in which the composition of a sample is determined. It is also a non-destructive method of analysis of the sample, and its operation is carried out by means of the fluorometer device. The principle of operation of the fluorometer is similar to that of the spectophotometer. However, an important difference between the two is

that the spectrophotometer plots exclusively reflect the absorption intensity value of the excitation wavelength absorbed by the sample. Whereas the fluorometer shows an emission spectrum of wavelengths of the sample excited by the desired beam. (17)

A fluorometer calculates the parameters that characterise different fluorescent materials, where in this particular condition we have the pigments alizarin red and alcian blue. These parameters are the intensity and the emission spectrum after excitation by a particular light spectrum.

Generally, it uses dual beams, which work together in harmony with the ultimate goal of reducing noise caused by fluctuations in radiation power. The upper beam shall pass first through a monochromator and then through the sample under examination. On the other side, the lower beam passes through an attenuator where it is adjusted to match the fluorescence power emitted by the sample. Finally, the light coming from the sample and the lower tuned beam are detected by separate tranducers, which convert them into an electrical signal, captured on the computer screen diagram.

More specifically, the transducer that detects the fluorescence of the upper beam is located at a distance from the cube chamber and at an optimal angle of 90° from the incident upper beam. It is designed to reduce the amount of stray light from the upper beam that can reach the detector. The convergence of the incident beam is carried out by the filters, where the broadband filter acts to reduce stray light, such as unwanted upper diffraction orders that will form in the monochromator.

It is well known that, as far as the question of the light source is concerned, a continuous source of radiation is required. Such a source is a Xenon arc lamp, which at the same time provides a wide range of excitation wavelengths.

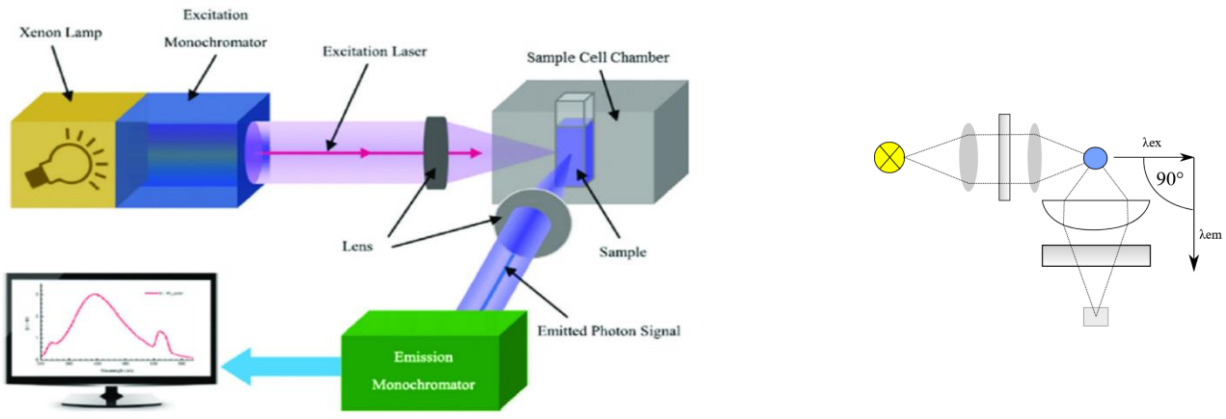

Figures 12: *Simplified experimental setups of a fluorescence spectrometer*

3.7 Sample Preparation

Firstly, we liquefied the 1% low-melting agarose mixture in the microwave and dropped a few drops of that warm solution on the curved surfaces of the skull, so that before it solidified we could more easily get rid of the bubbles in these areas of intense interest. After the first layer of agarose has been formed on the skull, a small layer is then added to the tube cap, where the level of the agarose will be slightly above the top of the tub. Allow it to cool for a while just long enough for this layer to form a solid base for the top of the skull. Finally, top up with agarose to just above the top of the sample and let it chill in the fridge.

When the sample is cooled and we are sure that there is no bubble in the agarose mixture, which may create some annoying scattering, we carefully unscrew the tube lid. We then place it with the help of the screw in the center of the lid into our specially designed stage, where the skull will be rotated. Finally, we have already filled a cube with deionized water, just below the stage in which it will be placed during the experiment. as shown in the pictures below.

Figure 13: *The tube in which the agarose mixture was placed, in which the biological samples were solidified.*

3.8 Two Dyes Spectrum (Fluorescence Origin Confusion Problem)

The case of the two skulls (S014, S024), where parts are impregnated with both pigments, is a bit special. In **figure 15**, the two fluorescence diagrams of the two dyes excited by a 488 nm beam are shown. The remarkable element and problem that we are asked to solve is that we are asked to solve is that in channel 2 (ch2), i.e., the 615/90 nm filter, strong fluorescence from both dyes appears. As a result, in the projections of these two skulls, due to this single fluorescence, there is confusion as to where it may be coming from. A typical example is the projection of S024, as shown in **figure 14**:

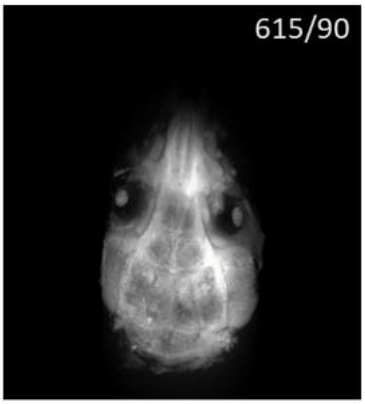

Figure 14: *The first projection of skull S024, stimulated by a 488nm laser beam.*

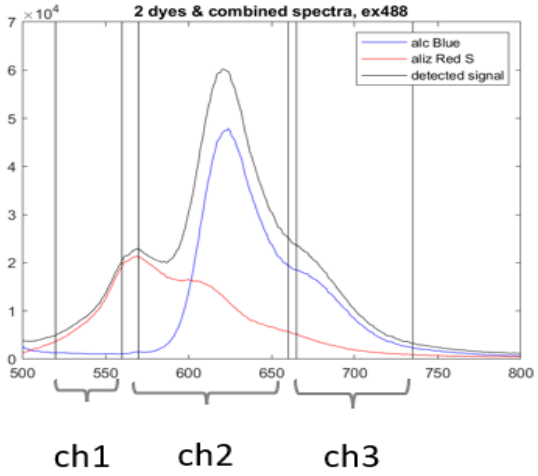

Figure 15: *The black curve describes the sum of the two color (blue and red) fluorescence curves of the two dyes by laser excitation at 488 nm. The vertical axis is the value of the emission intensity and the horizontal axis is the spectrum of the wavelength measured in nm. The red and blue curves represent the emission spectra, i.e. the fluorescence, of alizarin red and alcian blue, respectively. Below, the channels ch1, ch2 and ch3 represent the 540/40 nm, 615/90 nm, 700/70 nm filters which we choose each time to be the source of our information extraction.*

The problem of this inability to understand the origin of fluorescence was solved by the idea of unmixing, i.e. isolating and quantifying the information provided by each dye from each channel. More analysis is given in the next paragraph.

3.9 Cleaning up the Signal : Linear Unmixing in Fluorescence Microscopy

3.9.1 Introduction

Nowadays there is a richly diverse palette of fluorescent pigments available to scientific research, which have the ability to emit even outside the visible spectrum. However, there are several limitations concerning the identity of the fluorescent signals. Although for a simple external observer the signals of ordinary fluorophores can be distinguished from each other, the truth is that their distributions have a wide range and thus their contributions to the overall signal overlap with those of other pigments. Moreover, combinations of fluorophores will correspondingly lead to an unreliable separation.

The phenomenon of fluorescence in molecules refers to their ability to absorb photons of a certain energy and then immediately emit photons of lower energy. The photons that are absorbed have a specific energy that is determined within an energy spectrum, and the energy of those that are emitted must belong to a specific different spectrum. Knowing that energy is inversely proportional to wavelength, we then transpose the relationship so that it is described by the chromatic spectrum of light. A photon is absorbed by the molecule (towards the blue region) and a photon of longer wavelength (towards the red region) is emitted. The difference between the wavelength at which a fluorophore is most efficiently excited and the wavelength at which it emits as many photons as possible is called Stokes' shift. Beyond the maxima of the distributions, the excitation and emission spectra are spread out and fully described by a wider range of wavelength values, where the spectrum of the former describes the excitation efficiency at a given wavelength value, while the emission spectrum describes the probability of photon production at a given value. Moreover, as shown in **figure 16** below, the excitation and emission spectra exhibit mirror symmetry close to each other and even for well-defined fluorophores their range can span up to 100 nm, which for the visible light spectrum is sufficient.

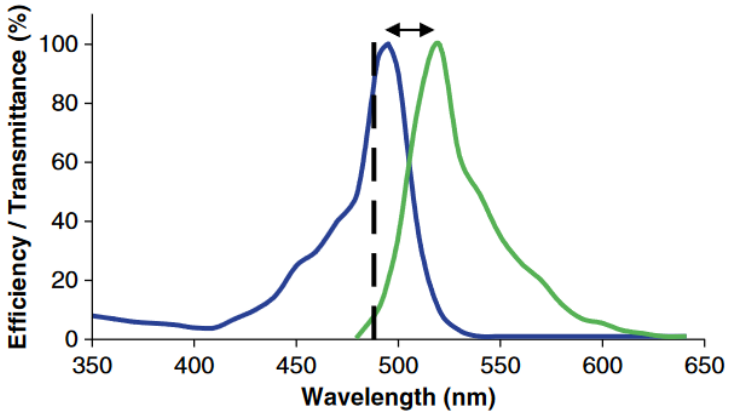

Figure 16

Fluorophore cross-talk is referred to as the overlap of the emission spectrum between the two fluorophores. More specifically, for a particular spectral region where the signal is detected, the

same will consist of the combination of the two fluorophores if and only if they are excited simultaneously. Fluorophore cross-excitation refers to the phenomenon of simultaneous excitation of both fluorophores due to the fact that at the maximum of the excitation spectrum of one, the second can be excited with a significant efficiency.

The use of appropriate set filters can lead to the successful separation of the fluorescence signals of the most common combinations of fluorophores. The shape of the spectra prepare the ground for such a separation. More specifically:

i. Excitation Spectrum: Forms a long tail towards the lower wavelength values, and shows a vertical drop after the maximum excitation value
ii. Emission Spectrum: It is mirror symmetric of the absorption spectrum, and thus exhibits a vertical rise towards the emission maximum following a tail towards the red region.

A good example to describe the simple separation of the signals of a mixed sample is the following. Consider a pair of fluorophores A and B which overlap, where the spectrum of B is slightly shifted towards the red region (to the right) relative to that of A. This will result in a possible cross-excitation of B with the excitation maximum of A. As can be seen in **figure 16**, at the low wavelength values in the emission spectrum of fluorophore A, where its emission maximum is formed, there can be no contribution from B, because fluorophore B starts to emit when its own emission maximum is formed. Thus, fluorophore A can be isolated from B by means of a band pass filter, where only the emission spectrum of A is retained, without creating any overlap problem with B. On the other hand, in the region where the maximum emission spectrum of B is formed, a strong overlap with the tail of the emission spectrum of A occurs. This surprisingly does not affect the situation and the explanation is simple. In the same region of the above discussion, the excitation spectrum of dye A has become negligible due to its rapid decay, compared to that of fluorophore B which is excited to its own maximum without the simultaneous excitation of A. (18)

The above case is the most common solution to the problem of separating the signal of a mixed sample in fluorescence microscopy. However, there are conditions under which the separation becomes more complex and the usual tools are inadequate. Such conditions are:

- When there is a particularly high number of wearables.
- In time-limited situations (e.g. in vivo imaging)
- When the fluorophores of interest are not compatible with existing filter sets.

The first hypothesis could easily be derived from an example (karyotyping using multicolor fluorescent in situ hybridization) of chromosome identification in which a large number of fluorescent signals are naturally required.

For the second condition, it is observed that in the in vivo experiments the acquisition time of the images is quite limited. More specifically, during the acquisition of the projections the shape of the sample under study may change. Moreover, when we have more than one

channel the acquisition of projections of the sample has to be done sequentially. This means that the more channels there are, the longer the time required will be. Thus, in the end the information obtained from the fluorescence channels of the live sample will not match each other perfectly.

And finally, our problem with the usual way of separating the signal concerns the last condition, which can be explained, for example, by genetically standard encoded proteins. Having fluorescent proteins in the 'portfolio' that provide a broad spectral distribution, often do not match the available fluorescence filter combinations and can hardly be mixed solely on the basis of spectral properties, due to their complex properties (pH, brightness, etc.).

In recent years, the use of the linear unmixing method for spectral data analysis and signal separation has become widespread and comes to overcome all the above mentioned problems.

3.9.2 Linear Unmixing

A general truth is that the fluorescence signals of the sample are a mixture of contributions from individual fluorophores that cover the entire volume. It is obvious that the total signal obtained is profoundly dependent on the concentrations of fluorophores. It is worth noting that if we were to observe portions of the total signal corresponding to different fluorescence channels, it would appear that the relative contributions of fluorophores vary with the distribution of emission spectra, regardless of fluorophore concentration. Linear Unmixing aims to determine the relative contribution from each fluorophore of each pixel in the image.

As a linear equation, the basic idea of the unmixing technique is based on Eq:

$$\mathrm{T}(\lambda) = A_1 \cdot Flu_1(\lambda) + A_2 \cdot Flu_2(\lambda) + A_3 \cdot Flu_3(\lambda) + \cdots \qquad (20)$$

where *T* corresponds to the total signal detected for each λ channel, Flu_x corresponds to the spectral contribution of each fluorophore in each λ channel, and A_x represent the abundancies (i.e., concentrations, proportions) of fluorophores in the regions of interest.

The above equation can also be written in the most general form:

$$T = \sum_{i=1} A_i \times R_i(\lambda) \qquad (21)$$

where *R* represents the reference emission spectrum of fluorophores. The fundamental principle underlying the calculations of linear unmixing is quite simple. Knowing all the reference emission spectra R of the fluorophores, through the above equation, the abundances A are calculated from the measured total signal.

In our case, we will use the method to explore the way in which individual fluorophores can be identified within a complex mixture in the double-labelled sample s024 (alcian blue + alizarin red). The black curve represents the summed spectrum, the red curve represents the fluorescence of alizarin red and the blue curve represents alcian blue.

Each pixel in the spectral image is categorized as a mixture of a fluorophore intensity signals when the measured spectrum can be deconstructed into the proportion, weight, or concentration of each individual fluorophore spectrum ($\mathbf{AlizRed}(\boldsymbol{ch_x})$, $\mathbf{AlcBlu}(\boldsymbol{ch_x})$) when the values are summed. First, we can study the case of excitation of the dyes by a 488 nm wavelength beam. We can distinguish two cases, for each excitation beam. If in both cases channel 1 will be our main source of information for the alizarin red dye, in the first of them we considered the ch_2 channel as the source of fluorescence pumping, while for the second case we included the filter of ch_3. The linear equation describing the system is:

$$\mathrm{T}(ch_x) = A_1 \cdot \mathrm{AlizRed}(ch_x) + A_2 \cdot \mathrm{AlcBlu}(ch_x) + offset_x \ , \ x = 1,2,3 \qquad (22)$$

where $T(ch_x)$ is the total signal obtained from each projection of the skull, or the total measured spectrum in the ch_x channel, $\mathrm{AlizRed}(ch_x)$ and $\mathrm{AlcBlu}(ch_x)$ represent the spectral contributions of each fluorophore in each channel ch_x, A_1, A_2 represent the abundancies of these two fluorophores. Finally, $offset_x$ is the fluorescence coming from an unpainted skull.

We easily calculated the areas occupied by each fluorescence in each channel, as shown in cases 01 & 02 below.

As we can observe the intensity of each pixel (***T***) in the spectral image is recorded when taking the stack of wavelengths. However, for this technique to work properly, it is necessary to record individual emission spectra (Reference Spectra) on separately prepared control samples for each fluorophore using identical sample preparation techniques and instrument settings. The overall spectral contributions of fluorophores in the sample can then be determined as a simple linear algebra exercise by calculating their individual contributions at each point in the measured spectrum (A_1, A_2) as the equation above. From linear mixing software packages the solution is achieved by introducing reference spectral profiles and using an inverse least squares fitting approach that minimizes the quadratic difference between the measured and calculated spectra.

3.9.3 Requirements for The Linear Unmixing

In order to attest that the application of the linear unmixing system, certain experimental criteria must be met. A key criterion is to ensure that the number of spectral detection channels is equal to or greater than the number of fluorophores, as we have correctly carried out. If this condition is not met, then it will not be possible to find a single result and multiple solutions will be obtained in the spectral separation calculation.

A second significant requirement, which allows the calculation of the fluorophore contributions, is the knowledge of the reference spectra of the fluorophore constituents of the sample. In addition, in order to exploit the method with maximum accuracy, reference spectra should be obtained from samples containing exclusively each fluorophore of interest. They may also be obtained in mixed samples provided that these specific regions are composed of the signal of interest, although there is always the risk that other fluorophores may contribute to the overall signal.

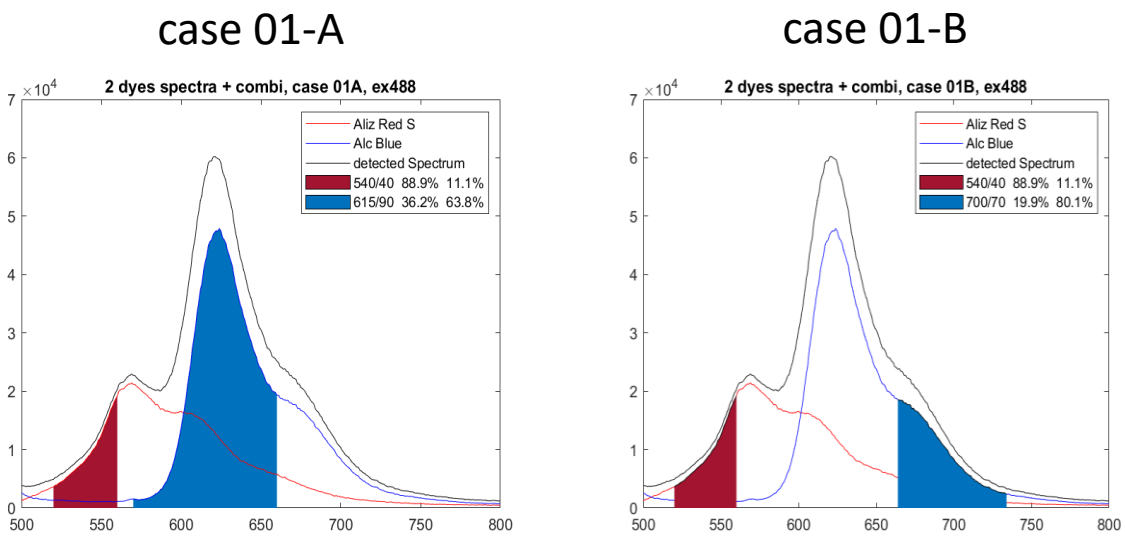

***Figure 17**: **(a)** It is the first hypothesis and is plotted exactly like the figure, except that we have calculated the fluorescence distributions occupied by each dye in each channel (ch_1 και ch_2), excited by a 488 nm wavelength laser beam. In the ch_1 channel, the area of the emission curve of alizarin red with respect to the total fluorescence is 88.9% (thus 11.1% of the total fluorescence comes from alcian blue) and in the ch_2 channel, respectively, the area of the emission curve of alcian blue occupies 63.8% of the total fluorescence. **(b)** Similarly, for case 02, in ch_3, 80.1% of the total skull fluorescence consists of alcian blue.*

We can observe in the fluorometer the same example for a 514 nm excitation laser beam. The following diagrams show our results:

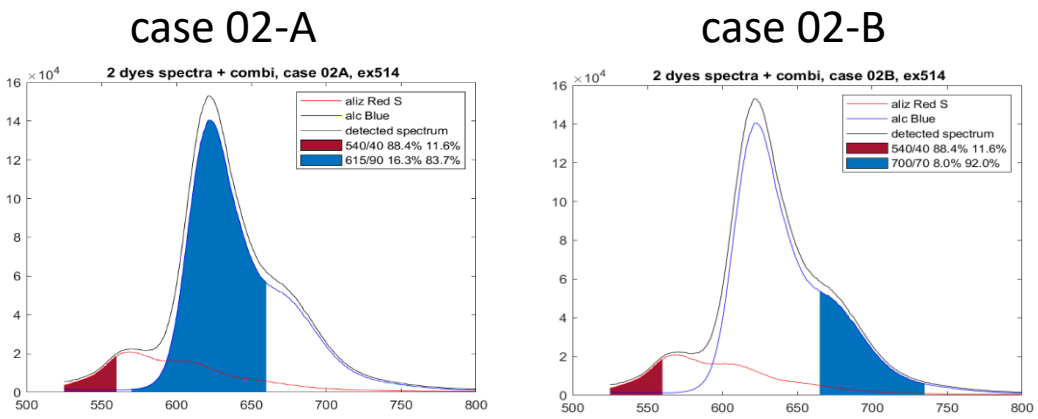

Figure 18: *Similar to* ***figure 17****, are the corresponding fluorescence contribution diagrams for excitation with a 514 nm laser beam.****(a)*** *Using the 540/40 nm channel, the skull's fluorescence is almost exclusively from alizarin red (88.4%), while the second spectrum of the 615/90 nm band-pass emission filter 615/90 nm is dominated by alcian blue (83.7%).* ***(b)*** *Same for the second diagram* ch_1 *-> alizarin red (88.4%) and* ch_2 *-> alcian blue (92.0%).*

3.9.4 Linear Unmixing Problems

An important problem that needs to be addressed in fluorescence microscopy on biological samples is their autofluorescence. The range of its spectrum distribution is quite large, so that it cannot be isolated from the spectrum of the signal of interest simply by using band-pass filters. In addition, the autofluorescence signal may emit with enough intensity to mask the weakest fluorescence in the sample. Thus, it can be expressed as an additional separate emission spectrum and defined as an additive term in the linear equations. In this way we achieve removal of the unwanted signal, originating from autofluorescence, from the image channels.

3.10 Assessment of Image Quality with Projection Number

It is well known that the quality of image reconstruction depends significantly on the number of views taken from different angles in the sample. The fewer these projections, during rotation, the more possible errors there will be in the reconstruction. Although for more projections, in which the depth of field ought to cover at least half the thickness of the sample, we have considerably greater accuracy in reconstruction, there are some limitations to be considered in the number of these. Longer laser exposure times can cause photobleaching effects, thus destroying the fluorescent properties of the samples.

For this very reason we chose, in our MATLAB code, to set the number of projections to 180, i.e. 1 projections per 2 degrees. It is worth noting that because the diameter of our beam on

both lasers was close to 15mm and the height of the samples is 25mm, we necessarily performed twice for each sample, once for the top and once for the bottom.

4. Results

4.1 Projections

As mentioned in the experimental procedure, through our CCD camera and layout we obtained 180 projections for each skull sample during rotation. For each laser beam that excited the respective dye, we changed the camera filter and repeated the same course of action. Below, the first images for each specific case are shown.

In total, we obtained for the 6 different skulls, $6 \cdot ((2 \cdot 3 \cdot 180) + 180) = 7{,}560$ projections. Numbers 2 and 3 are the wavelength laser beams in the respective camera filters, plus 180 images for the He-Ne laser beam (635 nm) in the 700/70 nm filter.

It is perhaps reasonable to ask why we have not obtained images of our biological samples in the 615/90 nm and 540/40 nm filters when excited by the He-Ne laser. The answer to this question lies behind a previous observation in the absorption spectra. It is known that the 635 nm beam belongs to the red region. Moreover, pigments when excited by this beam fluoresce at wavelengths much longer than 640 nm. Therefore, all we would achieve with such a filter is to observe only the beam itself, whereas with the 540/40 nm filter we would see total darkness.

4.2 Project's Purpose & Way of Thinking

The main purpose of this work is to distinguish between cartilage and bone in the 3D reconstruction of the biological specimen. This will clearly distinguish the disease of craniosynostosis. The experiments conducted for emission Optical Projection Tomography were divided into three categories:

- **Case A** (Alizarin Red): In this case the samples we evaluated (S011 & S012) are only immersed with the phosphorus dye alizarin red. More specifically, only the skull bone region is covered and the information obtained from one of these samples is strongly shown in the first projection in **figure 19**. It was excited by the Ar+ laser tuned at 488 nm by isolating the emitted radiation in the 665-735 nm region using a band-pass emission filter. It is considered the most ideal case to better highlight the bone. This can be demonstrated by the excitation and emission diagrams of this particular dye analyzed earlier in **figure 10(a) & 10(b)**, respectively. It is easy to notice the gaps formed in between the intense fluorescence coming from the dye. This gap is required to be filled by the second part which was the subject of our experiments.

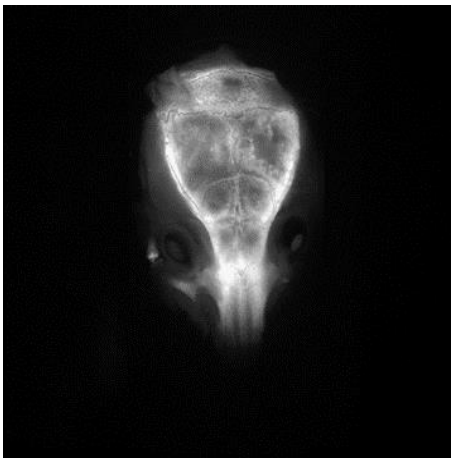

Figure 19: *The first projection of sample S011 taken from the CCD camera with a 700/70 nm band-pass emission filter mounted on top, where the alizarin red dye is excited by a 488 nm laser beam.*

An example of case A, in which the T-OPT and F-OPT 3D reconstructions can be clearly shown, is the following:

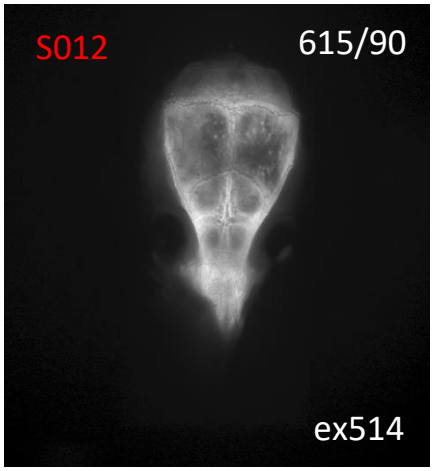

Figure 20: *S012, excitation beam 635 nm, band-pass emission filter 700/70 nm*

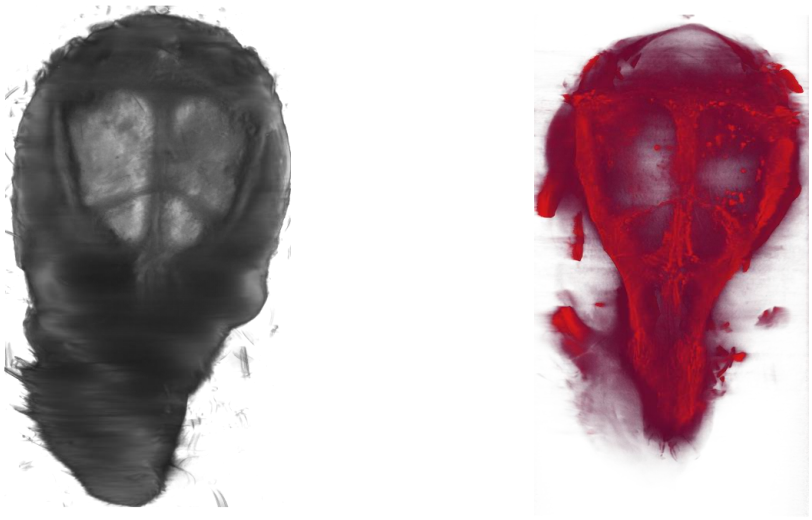

(a) **(b)**

Figure 21:* (a)** *T-OPT mode 3D reconstruction of S012 mice skull. The geometry of the T-OPT simply shows the contour of the sample.* ***(b) *F-OPT mode 3D reconstruction. The bone area can be seen quite clearly.*

The only problem that can be identified in this case is that the fluorescence of Alizarin Red fluorophore was detected only by channel 2 (615/90 nm) and almost not at all by channel 1 (540/40 nm). This cannot be justified by the emission spectrum of this dye, since it emits quite strongly there and at the same time the skull is only stained with this fluorophore.

- **Case B** (Alcian Blue): In the second case in the two skulls (S015 & S025) the cartilage area was coated with the phosphorus pigment alcian blue, with no other pigment added to any other area, or so it was assumed. We will discuss in a following paragraph what is implied by this phrase. Similarly, one of the two samples (S025) was chosen to be imaged in this paper, and the first projection obtained is shown in **figure 22**. The contrast between the cartilage crossing the area of the bone is clear. According to the excitation and emission diagrams in the **figure 11(c) & 11(d)**, intense photon excitation of the dye and a satisfactory emission in the 665-735 nm region.

However, a fairly large problem of distinguishing cartilage from bone was reflected in the remaining images. More specifically, as highlighted in **figure 19**, there is very intense fluorescence in the tissue around the perimeter of the skull and hardly any in the desired area of the cartilage lines. As highlighted in the alcian blue emission spectrum, there is strong photon emission in the 575-650 nm region of the fitted band-pass emission filter, which does not explain the so low information drawn from the cartilage.

A possible explanation for this phenomenon is the possible immersion of even the soft tissue surrounding the skull. As a result, the laser beam excites photons in that area as well and then the corresponding radiation is emitted. Otherwise, it may constitute autofluorescence of the soft tissue itself, which will be a limitation that will be a concern for Linear Unmixing in the following and final case.

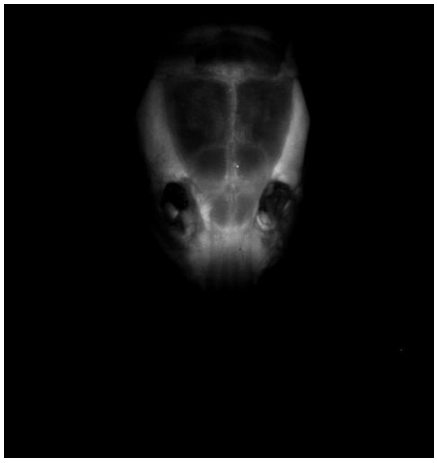

Figure 22*: The first en face projection of sample S025, with the alcian blue dye excited by a 635 nm laser beam and the information isolated by a 700/70 nm band-pass emission filter.*

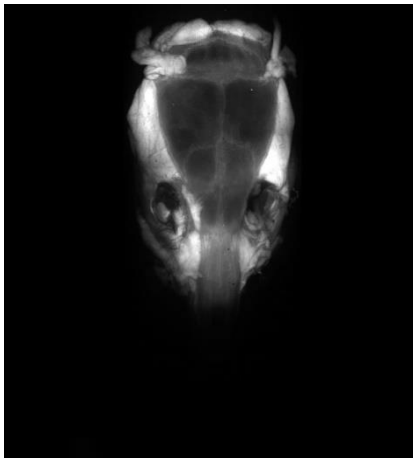

Figure 23*: Projection of sample S025, excited by a 514 nm laser beam, with a 700/70 nm band-pass emission filter. The cartilage lines are faintly depicted, in contrast to the surrounding soft tissue.*

An example of case B, in which the two 3D reconstructions can be clearly shown, is the following:

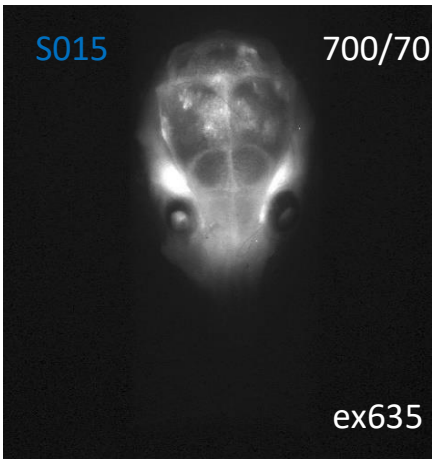

Figure 24: *S015, excitation beam 635 nm, band-pass emission filter 700/70 nm*

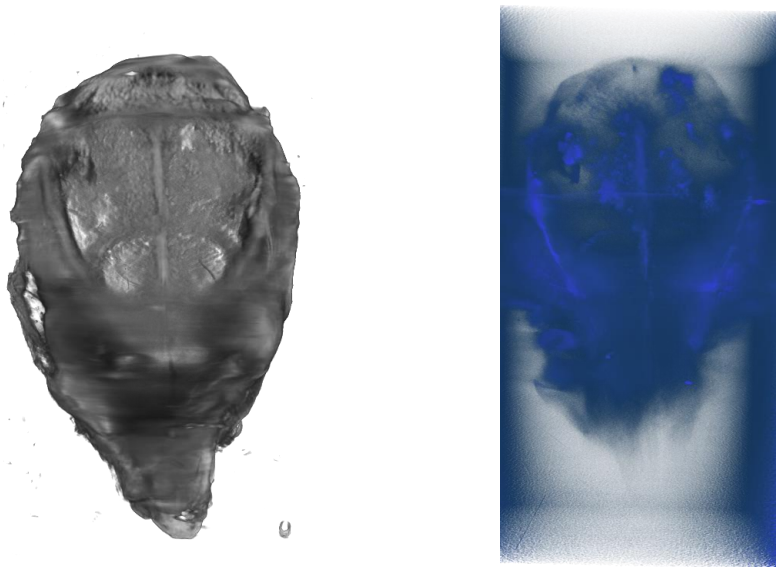

(a) **(b)**

Figure 25: **(a)** *T-OPT mode 3D reconstruction of S015 mice skull* ***(b)*** *F-OPT mode 3D reconstruction. The contrast of the cartilage that crosses the bone is noticeable.*

- **Case A+B** (Alizarin Red + Alcian Blue): In the third and last case, the two mice skulls were color treated with both dyes in the respective regions. Alizarin red in the bone region and Alcian Blue at the cartilage border. This case is the most important one. In

these two samples (S014 & S024), the two different fluorophores were combined to emit each dye from the respective desired one.

Unfortunately, a similar problem was encountered with the case of alcian blue fluorescence in cartilage (**case B**), but this time on the side of Alizarin Red. More specifically, the information received from the bone region is zero. Instead, once again, the radiation coming from the soft tissue is very bright.

4.2.1 Problematic Results

Assuming that the fluorophore has correctly coated the biological sample, this picture does not match reality. This is because, according to the excitation and emission spectra of the two dyes in **figure 18**, the photons of alizarin red are overwhelmingly more strongly excited and are considered the absolute dominant in the emission of the sample compared to alcian blue. This logical association is not confirmed by the **figure 26**.

The paradox that was created is probably explained by the incorrect immersion of the skull. It is possible that the dye passed into the soft tissue around the skull. Subsequently, a problem will also arise in the 3D reconstruction of the same specimen. Otherwise, there may be some kind of autofluorescence. More specifically, in **case A+B** the linear unmixing method was applied, which aims to separate the signals coming from the two different fluorophores. The autofluorescence of the skulls hinders the detection and accurate quantification of the fluorophores during imaging. The emission spectra of autofluorescence may overlap with those of exogenous fluorophores, making it difficult to distinguish the desired signal from background noise.

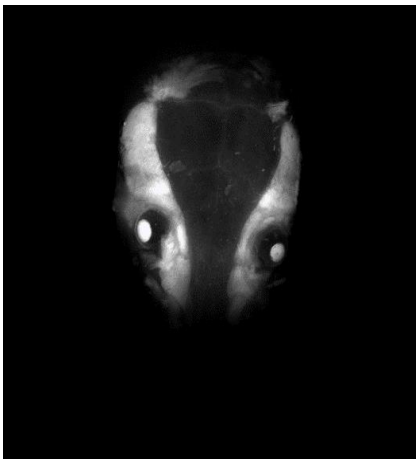

***Figure 26**: First projection of s014 sample, excited by laser beam 514 nm with band-pass emission filter 540/40 nm. The signal coming from the soft tissue, unfortunately, takes center stage, leaving the parts of the bone dark.*

4.2 3D Reconstruction

The collected projection images are processed and reconstructed using computational algorithms to create a 3D representation of the internal structures within the skull. These

algorithms use mathematical techniques, which were discussed above, such as Radon Transform, to convert 2D projections to 3D visualization.

4.2.1 Volume Rendering

After the reconstruction of the 3D volume, it can be presented using volume rendering methods. This procedure involves mapping the reconstructed voxel values to colors or opacity values to create a 3D visualization that provides insights into the internal structures of the sample. The 3D reconstructions can be observed through specialized software tools, which facilitate an interactive investigation of the internal structures within the sample. These software applications enable researchers to manipulate the 3D volume by rotating and zooming it, providing the means to closely examine particular areas of interest. The software in which our samples were given a beautifully processed 3D format is AMIRA Resolve RT. There, the form of the cartilage as well as that of the rest of the bone can be shown thoroughly with different color palettes.

In the results, sample S014 was selected, which is immersed by both fluorophores. After successive tests combined with the information one can obtain from the emission and excitation diagrams, the best possible set of image packets is:

	Excitation Laser beam (nm)	**Band-pass emission filter (nm)**
Cartilage	635	700/70
Bone part	514	700/70

The projection sets were combined, initially in the ImageJ application, to clearly illustrate which ones would be best matched for reconstruction and at the same time to present a first glance of the contributions of the fluorophores. In green is shown the region excited by a 635 nm beam, where a 700/70 nm band-pass emission filter is mounted on the CCD camera lens and characterizes the cartilage part, while the red region was excited by a 514 nm beam and the desired information characterizing the bone region was isolated with a 615/90 nm band-emission filter (**figure 27(b)**). In addition, we collected the projections of sample S014 derived from light absorption (T-OPT) and the first projection is shown in **figure 27(a)**. It is easy to see that, just as we discussed in the theory, the deeper tissues, i.e., cartilage and the outer sheath are the darkest regions of the skull since they absorb more radiation themselves.

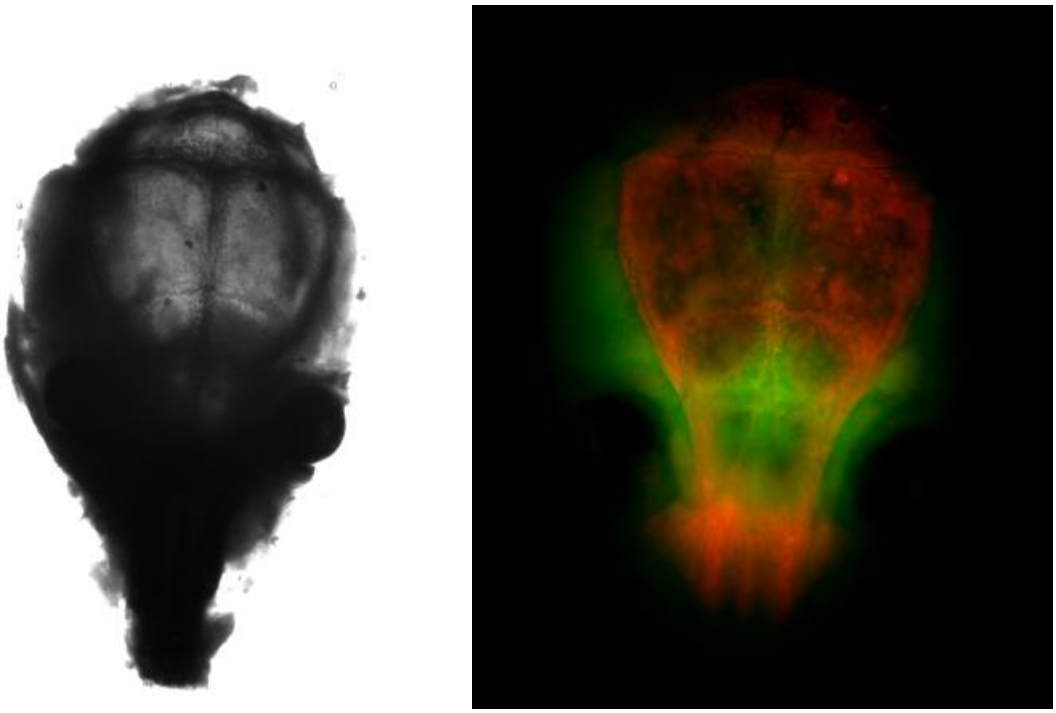

(a) **(b)**

Figure 27: (a) *The first projection of the skull exposed in front of a uniformly distributed white light absorbing it following the Beer-Lambert law.* ***(b)*** *The first projection of sample S014 is shown. The green line in the middle of the skull represents the part of the cartilage that fills the gap left by the part of the bone.*

4.2.2 T-OPT & E-OPT 3D Reconstructions

First, we will present the result of the 3D reconstruction of the t-OPT mode, as shown in **figure 28**. It is worth noting that the importance of transmission OPT stands on the formation of the sample contour. It cannot highlight and emphasize the details of each structure that make up the skull. This bridging comes to be covered through the e-OPT mode.

In the 3D reconstruction of the e-OPT mode, which is shown in **figure 29**, the information obtained from the excitation of the sample by a 514 nm laser beam with a 540/40 nm band-pass emission filter is set in red in AMIRA. This fluorescent region belongs to the bone with some obvious extra details compared to the t-OPT mode. However, this reconstruction has also been combined with excitation by a 635 nm laser beam with a band-pass emission filter 700/70 nm, green to blue. The fluorescent blue line crossing the bone volume and representing the cartilage can be seen. Of course, there are other areas that characterize the cartilage and due to the dye deposition issues discussed above, they were not strongly seen or not seen at all.

Figure 28: *3D reconstruction of the skull in t-OPT mode. The general shape of the specimen is shown with a minimal detail revealing the thickness of the area of high interest.*

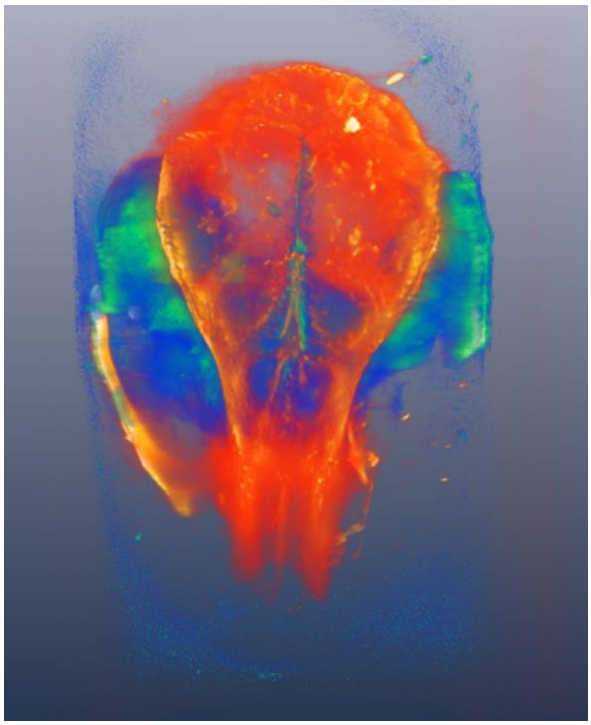

Figure 29*: 3D reconstruction of the s014 sample in e-OPT mode.* ***i)*** *The information obtained from a 635 nm laser beam and a 700/70 nm band-pass emission filter is shown in green and blue. The fine lines crossing the bone section are quite clear.* ***ii)*** *The red and slightly yellow*

colour represents the part of the bone, which was excited by a 514 nm laser beam and the fluorescence was isolated by a 700/70 nm band-pass emission filter.

5. Conclusion

In these continuous experiments, the method of optical projection tomography was studied in detail. The technique was divided into two methods, the t-OPT mode, which calculates the light absorption of the specimen, and the e-OPT mode, in which the fluorescence of the skull is calculated. More specifically, the theory for 3D reconstruction was developed, such as Radon transform, where the collected projections represent the light passing through the specimen from the specific angle creating a radon matrix. The Central Slice Theorem comes to unite the Fourier transform (frequency) of the sample transparency with the corresponding Radon transform of the Radon matrix. Finally, the Filtered-back projection method is used to actually reconstruct the sample from the projections, revealing its internal structure and composition. In addition to the optical projection tomography method, simultaneous fluorescence coming from two different fluorophores was studied by giving different stimuli to them, such as laser beams, and having different ways to obtain their emission, such as band-pass emission filters. Then, using the linear unmixing method, the fluorescence of the fluorophores of the samples was separated and its origin was determined. This ultimately results in the discrimination of the cartilage over the bone region, as can be seen in the 3D reconstruction of the skull, which is the problem area of craniosynostosis disease.

6.References

1. **Cheriyedath, Susha.** Micro-MRI Principles, Strengths, and Weaknesses: NEWS Medical Life Sciences. [Online] February 26, 2019. https://www.news-medical.net/life-sciences/Micro-MRI-Principles-Strengths-and-Weaknesses.aspx.

2. **Nguygen, David.** *David NGUYEN Thèse N° 9094 Optical projection tomography for whole organ imaging.*

3. **Sharpe, James.** Optical projection tomography as a new tool for studying embryo anatomy. *Journal of Anatomy.* February 2003, pp. 175-181.

4. **UCL.** Optical Projection Tomography: UCL. [Online] https://www.ucl.ac.uk/centre-for-advanced-biomedical-imaging/imaging/techniques/optical-projection-tomography.

5. **Braden G, Knapp H, FitzGerald G, Marcus A, Weksler B, Jaffe E, Broekman M, Sharpe J, Ahlgren U, Perry P, Hill B, Ross A, Hecksher-Sørensen J, Baldock R, Davidson D.** *Optical Projection Tomography as a Tool for 3D Microscopy and Gene Expression Studies.* 1976.

6. **Wikipedia.** Craniosynostosis: Wikipedia The Free Encyclopedia. [Online] https://en.wikipedia.org/wiki/Craniosynostosis.

7. **JOHNS HOPKINS MEDICINE.** Craniosynostosis: JOHNS HOPKINS MEDICINE. [Online] https://www.hopkinsmedicine.org/health/conditions-and-diseases/craniosynostosis.

8. **Bryan, Peter Barrett.** The Radon Transform: Basic Principle. [Online] April 25, 2022. https://towardsdatascience.com/the-radon-transform-basic-principle-3179b33f773a.

9. **Weisstein, Eric W.** Radon Transform: MathWorld. [Online] https://mathworld.wolfram.com/RadonTransform.html.

10. **Hayden, Brendan F.** Slice Reconstrunction . [Online] October 2, 2005. https://homepages.inf.ed.ac.uk/rbf/CVonline/LOCAL_COPIES/AV0405/HAYDEN/Slice_Reconstruction.html.

11. **Maligs F, Murphy A, Bell D.** Filtered back projection. *Radiopaedia.* June 12, 2016.

12. **Onur, Tuğba Özge.** An application of filtered back projection method for computed tomography images . *International Review of Applied Sciences and Engineering* . April 2, 2021, pp. 194-200.

13. **National Center for Biotechnology Information.** Ram Lak Shepp Logan figure: An Introductory Guide: National Center for Biotechnology Information. [Online] https://www.ncbi.nlm.nih.gov/books/NBK546157/figure/ch8.fig13/.

14. ***Laser Beam "Clean-Up" with Spatial Filter.*** **s.l. : VirtualLab Fusion Basic, 2020.**

15. THORLABS. Spatial Filters Tutorial: THORLABS. [Online] https://www.thorlabs.com/newgrouppage9.cfm?objectgroup_id=10768.

16. Βικιπαίδεια. Φασματοφωτόμετρο: Βικιπαίδεια. [Ηλεκτρονικό] https://el.wikipedia.org/wiki/%CE%A6%CE%B1%CF%83%CE%BC%CE%B1%CF%84%CE%BF%CF%86%CF%89%CF%84%CF%8C%CE%BC%CE%B5%CF%84%CF%81%CE%BF .

17. Wikipedia. Fluorometer: Wikipedia. [Online] https://en.wikipedia.org/wiki/Fluorometer.

18. Zimmermann T, Marrison J, Hogg K, O'Toole P. Clearing up the signal: Spectral imaging and linear unmixing in fluorescence microscopy. *Methods in Molecular Biology.* 2014, pp. 129-148.

19. Wikipedia. Optical Projection Tomography: Wikipedia. [Online] https://en.wikipedia.org/wiki/Optical_projection_tomography.